Journal of Digital Imaging (2023) 36:879–892
https://doi.org/10.1007/s10278-022-00759-9

ORIGINAL PAPER

Automated Adrenal Gland Disease Classes Using Patch-Based Center Symmetric Local Binary Pattern Technique with CT Images

Suat Kamil Sut[1] · Mustafa Koc[2] · Gokhan Zorlu[3] · Ihsan Serhatlioglu[3] · Prabal Datta Barua[4,5] · Sengul Dogan[6] · Mehmet Baygin[7] · Turker Tuncer[6] · Ru-San Tan[8,9] · U. Rajendra Acharya[10,11,12]

Received: 15 October 2022 / Revised: 9 December 2022 / Accepted: 13 December 2022 / Published online: 19 January 2023

Abstract
Incidental adrenal masses are seen in 5% of abdominal computed tomography (CT) examinations. Accurate discrimination of the possible differential diagnoses has important therapeutic and prognostic significance. A new handcrafted machine learning method has been developed for the automated and accurate classification of adrenal gland CT images. A new dataset comprising 759 adrenal gland CT image slices from 96 subjects were analyzed. Experts had labeled the collected images into four classes: normal, pheochromocytoma, lipid-poor adenoma, and metastasis. The images were preprocessed, resized, and the image features were extracted using the center symmetric local binary pattern (CS-LBP) method. CT images were next divided into 16 × 16 fixed-size patches, and further feature extraction using CS-LBP was performed on these patches. Next, extracted features were selected using neighborhood component analysis (NCA) to obtain the most meaningful ones for downstream classification. Finally, the selected features were classified using *k*-nearest neighbor (kNN), support vector machine (SVM), and neural network (NN) classifiers to obtain the optimum performing model. Our proposed method obtained an accuracy of 99.87%, 99.21%, and 98.81% with kNN, SVM, and NN classifiers, respectively. Hence, the kNN classifier yielded the highest classification results with no pathological image misclassified as normal. Our developed fixed patch CS-LBP-based automatic classification of adrenal gland pathologies on CT images is highly accurate and has low time complexity $O(w \times h + k)$. It has the potential to be used for screening of adrenal gland disease classes with CT images.

Keywords Adrenal gland · Center symmetric local binary pattern · Neighborhood component analysis · Classification

Introduction

Background

Adrenal lesions are not infrequently encountered in practice due to the ubiquitous use of cross-sectional diagnostic imaging. In addition, some adrenal lesions actively secrete hormones and manifest clinical symptoms and abnormal results on biochemical and endocrine function tests that draw attention to the diagnosis. In contrast, non-functioning adrenal masses can remain clinically dormant and present only as incidental findings on CT ("incidentalomas"). Indeed, adrenal masses are reported in approximately 5% of patients undergoing abdomen computed tomography (CT) examination [1].

Lipid-poor adenomas, pheochromocytomas, and metastases share similar CT morphological features and defy easy differentiation [2, 3]. To improve the diagnostic discrimination, it may be necessary to administer contrast media or use alternative modalities like magnetic resonance imaging (MRI), which offers more granular tissue characterization [2, 3]. Adrenal adenoma, the commonest adrenal tumor, may either be lipid-poor or, more frequently, lipid-rich [4]. Detection of intracellular lipids on CT or MRI reliably identifies the former [5], making it less of a diagnostic challenge. Unlike the rapid flushing of contrast media seen with lipid-poor adenoma, adrenal metastases tend to retain contrast and become enhanced. Pheochromocytomas are rare tumors arising from the adrenal medulla that occur either sporadically or as part of hereditary syndromes. While CT can help locate the pheochromocytoma and delineate local invasion or metastasis, it cannot definitively discriminate between pheochromocytoma and lipid-poor adenoma as both demonstrate similar tissue signals and rapid contrast washout behaviors [6, 7]. Pheochromocytoma can be catecholamine-secreting

✉ Sengul Dogan
sdogan@firat.edu.tr

Extended author information available on the last page of the article

or non-secreting. The former is associated with characteristic symptomatic paroxysms and even life-threatening hypertensive crises requiring early curative surgery. Both secreting and non-secreting pheochromocytomas have the potential for malignant transformation [8], underscoring the importance of accurate imaging diagnosis and continued surveillance. The adrenal glands are common sites for metastasis. Careful evaluation of adrenal masses in cancer patients is imperative as diagnostic confirmation of adrenal metastases will upend prognosis and treatment [9]. Features that distinguish malignant from benign adrenal masses include the presence of calcification, necrosis, hemorrhage, intracytoplasmic lipid, locoregional and distant disease, and, as mentioned, contrast enhancement.

The subtle permutations of tissue signals and morphological differences seen among the various types of adrenal lesions render them eminently amenable to machine learning (ML)-based classification. In [10], an ML model that performed texture analysis of CT images attained an average accuracy of 82% for differentiating between adrenal adenomas and carcinomas. In [11], another ML model using an ensemble extra tree classifier achieved 91% classification accuracy for indeterminate solid adrenal lesions. Moawad et al. [12] applied ML-based texture analysis to a dataset comprising CT images from 40 indeterminate small adrenal tumors. They reported 85% area under the curve, 84.2% sensitivity, and 71.4% specificity with their method. Romeo et al. [13] developed a model with a J48 classifier for texture analysis of MRI images and achieved 80% diagnostic classification accuracy for lipid-rich, lipid-poor, and non-adenoma adrenal lesions. Yi et al. [14] used texture analysis to differentiate between lipid-poor adenoma and pheochromocytoma in a dataset of CT images derived from 108 patients with adrenal incidentalomas. The model achieved 94.4% accuracy, 86.2% sensitivity, and 97.5% specificity. The number of ML studies in the literature on adrenal masses is limited; most of them are based predominantly on texture analysis. In this study, a highly accurate model was developed to classify adrenal masses using an innovative patch-based operation to generate more image features, and the model was tested on a new CT dataset.

Motivation and our Method

Nowadays, deep learning (DL) and ML-based methods are approaches used in many classification problems [15, 16]. ML-based biomedical image classification has become a popular area of research [17–20]. Computer-aided diagnosis systems have been increasingly used in diverse healthcare applications [21, 22]. In this study, a new handcrafted ML method was developed for the automatic classification of adrenal gland images that was inspired by image division-based methods like vision transformer (ViT) [23] and multilayer perceptron mixer (MLP-Mixer) [24], which have yielded excellent performances in the field of computer vision. The model developed in this study has lower computational complexity than other models using DL [25]. First, regions of interest (ROI) were automatically segmented from the acquired raw images to delineate the boundaries of the body section showing the adrenal glands. The segmented images were then divided into fixed-size patches, and feature extraction was performed on each patch using the fast and simple center symmetric local binary pattern (CS-LBP) method. The neighborhood component analysis (NCA) [26], a well-known feature selection function, was then applied to the resultant feature vector. The most significant and distinctive features were thus selected, and the size of the feature vector was reduced. Next, the selected features were classified using standard classifier *k*-nearest neighbor (kNN) [27], support vector machine (SVM) [28, 29], and neural network (NN) [30]. Among these, kNN and SVM [31] were optimizable, and Bayesian optimization [32] was used to determine their hyperparameters. All three classifiers were developed using ten-fold cross-validation (CV) with 100 iterations.

Main Contributions

The main contributions of this handcrafted patch-based CS-LBP model are given below:

- Feature extraction was applied to the main image and divided fixed-size 16×16 patches. The feature extraction in this study is different than standard LBP [33]. Instead of neighboring pixels, symmetrical pixels were taken into account, which might have contributed to the success of our method.
- All three different classifiers achieved at least 98% accuracy, which attests to the fidelity of the upstream feature extraction.
- A new CT dataset was specially acquired and used in this study. This dataset has been published at https://www.kaggle.com/turkertuncer/surrenal-image-dataset.
- The handcrafted ML model has low time complexity, an important consideration for remote and real-time clinical applications.

Materials and Methods

Material

From CT examinations of 96 unique subjects who attended the Firat University Hospital, we collected 759 transverse cross-sectional image slices that contained views of the adrenal glands. These images were reviewed by medical

specialists and categorized into four classes: normal, pheochromocytoma, lipid-poor adenoma, and metastasis. Lipid-rich adenomas were not studied as they do not pose a diagnostic challenge. The dataset is downloadable from https://www.kaggle.com/turkertuncer/surrenal-image-dataset. Details of the dataset are summarized in Table 1. Typical images of all classes are shown in Fig. 1.

CS-LBP-Based Automatic Adrenal Gland Classification Model

The model consists of five steps: image segmentation; CS-LBP-based feature extraction; feature concatenation; feature selection with NCA; and classification using kNN, SVM, and NN. These steps are explained in the subsequent sections. First, a schematic representation of the model is shown in Fig. 2, and the pseudocode is given in Algorithm 1.

Herein, each image in the dataset is resized (224 × 224). The resized image is divided into 16 × 16 patches. (In other words, the 224 × 224 image was divided into small non-overlapping 16 × 16 images.) The main image and patches (a total of 196 patches) are given as input to the CS-LBP-based feature extractor. CS-LBP generates 16 features per image. A total of 3152 features are generated from the main image and patches (16 features from main images and 3136 features from patches). This process is done for 759 images in the dataset. A feature vector of size 759 × 3152 is obtained. The NCA algorithm is applied to this feature vector, and the 160 most distinctive features are selected. Finally, the selected features are classified.

Segmentation

This model was developed based on ViT and MLP-Mixer, and a preprocessing step was applied to crop every raw transverse CT image to the limits of the body section that contained the adrenal glands. The region of interest (ROI)-based image segmentation consisted of simple steps (Fig. 3) that had been chosen for their low complexity. First, the raw CT image was converted to grayscale. Next, a 25 × 25 median filter was applied. The boundaries were then determined using the thresholding method, and the image was segmented according to the boundaries. Finally, the segmented image was resized to 224 × 224.

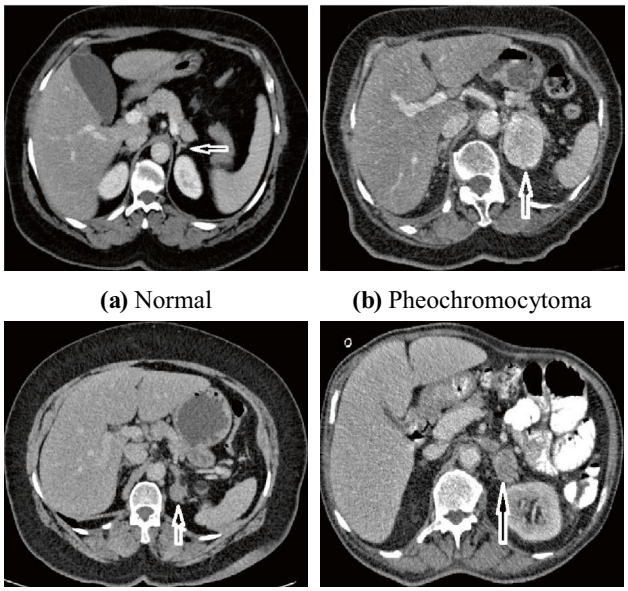

(a) Normal **(b)** Pheochromocytoma

(c) Lipid-poor Adenoma **(d)** Metastasis

Fig. 1 Sample adrenal gland images from all classes

The preprocessing steps are given below.

Step 0: Read CT images from the dataset.
Step 1: Apply ROI-based segmentation to the raw image.
Step 2: Resize the CT image to a 224 × 224-sized image.

Feature Extraction with the CS-LBP Method and Feature Concatenation

CS-LBP is an interest region descriptor that has high accuracy, especially in flat image areas. Instead of comparing each pixel value with the center pixel, it is compared with the symmetrically opposite pixel. The signum function is used in the comparison process. A block diagram summarizing this method is given in Fig. 4, and the pseudocode in Algorithm 2.

Table 1 The details of the dataset (759 images) used

Feature	Value
Image type	Computed tomography
Sex	59 males; 37 females
Age, years (range)	55.85 ± 15.2 (23–85)
Date range	01.12.2020 to 01.12.2021
Class (number of CT images)	0, normal (314); 1, pheochromocytoma (122); 2, lipid-poor adenomas (174); 3, metastasis (149)

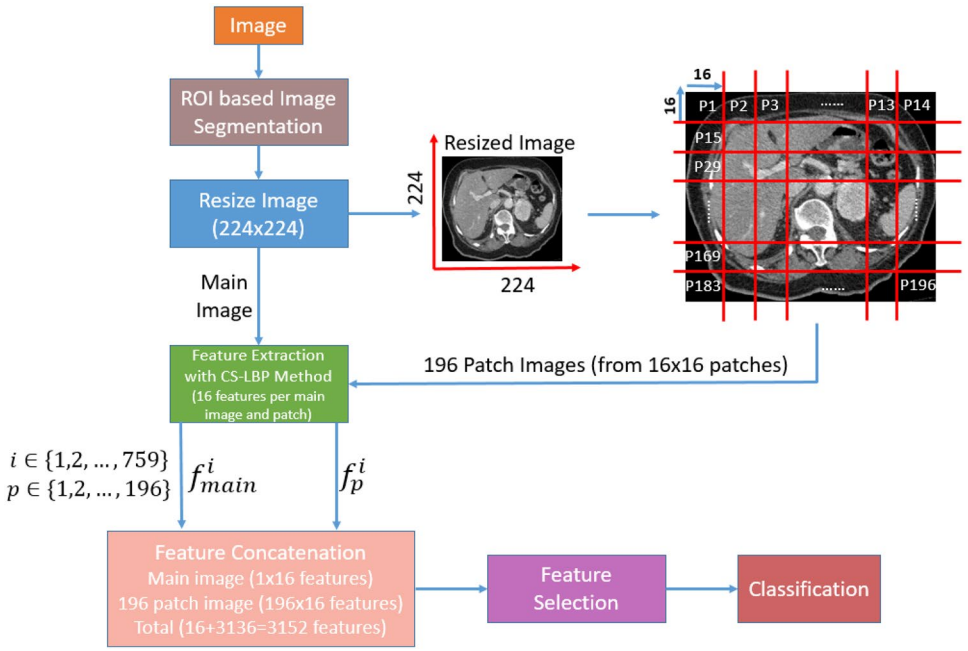

Fig. 2 Schematic overview of the patch-based CS-LBP technique

The CS-LBP method extracted 16 features from each resized 224 × 224 image. Next, the latter was divided into 196 fixed-size 16 × 16 patches, and features were extracted from each patch using the CS-LBP method. The steps of the feature extraction process are given below.

Step 3: Extract 16 features from a resized segmented image by using the CS-LBP method.
Step 4: Divide 16 × 16-sized patches into the image.

$$Patch^k = image(i+t-1, j+m-1), i \in \{1,17,33,\ldots,w\},$$
$$j \in \{1,17,33,\ldots,h\} t \in \{1,2,\ldots,16\}, m \in \{1,2,\ldots,16\},$$
$$k \in \left\{1,2,\ldots,\frac{w \times h}{16^2}\right\} \quad (1)$$

Input: Adrenal gland CT image. **Output:** Predicted values.
0: Load image.
1: Segment boundaries of the adrenal gland image.
2: Resize the segmented image to a 224 x 224 sized image.
3: Extract 16 features from resizing a segmented image by using CS-LBP.
4: Divide resized image into 16 x 16 sized non-overlapping patches (a total of 196 new images).
5: Extract 16 features from each patch by using CS-LBP.
6: Concatenate features and obtain 759 x 3152 features (Number of images: 759 and the number of features: 3152)
7: Apply NCA to concatenated 3152 features, and 160 most discriminative features are selected.
8: Classify reduced features and obtain predicted values.

Algorithm 1 Pseudocode of the proposed CS-LBP-based model

where $Patch^k$ is the k^{th} patch, i and j describe the indices of the image, and w and h are the number of rows and columns of the resized image.
Step 5: Extract 16 features from each patch by using CS-LBP (Algorithm 2).where $feat^{all}$ is the feature vector, $feat^{main}$ is the feature of the resized image from the first step, and "+" symbol denotes the concatenation operation. In this step, 16 features were obtained from the main image and 3136 (196 patches × 16 features) from the patches. Thus, a total of 3152 features were obtained.
Step 6: Concatenate features of each patch to obtain features.

$$feat^{all} = feat^{main} + Patch^1 + Patch^2 + \cdots + Patch^k \quad (2)$$

where $feat^{all}$ is the feature vector, $feat^{main}$ is the feature of the resized image from the first step, and "+" symbol denotes the concatenation operation. In this step, 16 features were obtained from the main image and 3136 (196 patches × 16 features) from the patches. Thus, a total of 3152 features were obtained.

Neighborhood Component Analysis-Based Feature Selection

Feature selection optimizes classification performance by selecting the most distinctive features and reducing model computational costs. The NCA [26] is a supervised feature selection algorithm that aims to maximize the prediction accuracy of classification algorithms. This algorithm is a feature selection version of the kNN algorithm and works

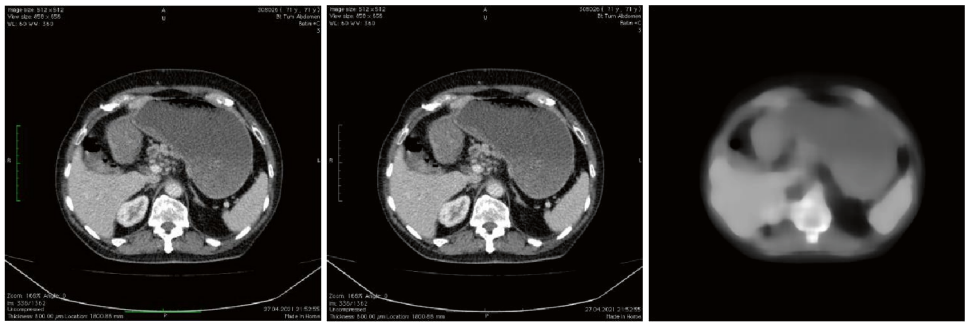

(a) Raw CT image **(b)** RGB2Gray **(c)** Median filter

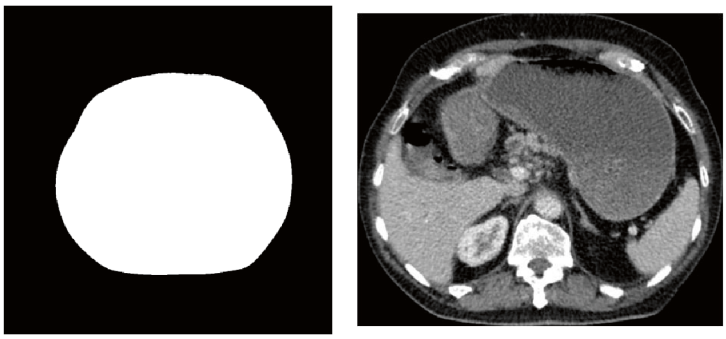

(d) Threshold and detect boundaries **(e)** Segmented image

Fig. 3 ROI-based image segmentation steps

based on distance. The NCA algorithm takes the feature vector (predictors) and responses (labels) as input parameters and calculates the weight of each feature column. It uses the Stochastic Gradient Descent (SGD) algorithm to estimate feature weights and generates only positive weight values. This is because higher weights imply more meaningful features. In this paper, 160 features with the highest weight values were selected from the extracted 3152 features from each image. The weight of the top 160 features with the highest rank is shown in Fig. 5. The 160 features were determined by prior trial and error.

Step 7: Select features with NCA.

$$\begin{aligned} weights^{NCA} &= NCA(feat^{\text{all}}) \\ ind &= argsort(weights^{NCA}, descending) \\ sf(i) &= feat^{\text{all}}(ind(i)), i \in \{1, 2, 3, \ldots, 160\} \end{aligned} \tag{3}$$

where $weights^{NCA}$ denotes the weights of features, *ind* shows an index of the sorted qualified features, and *sf* means the selected features.

Classification

We tested the model performance using kNN [27], SVM [28, 29], and NN classifiers [30]. Ten-fold CV was used in all experiments with 100 iterations. The classification step is given below.

Step 8: Classify the selected features using kNN, SVM, and NN with a 10-fold CV.

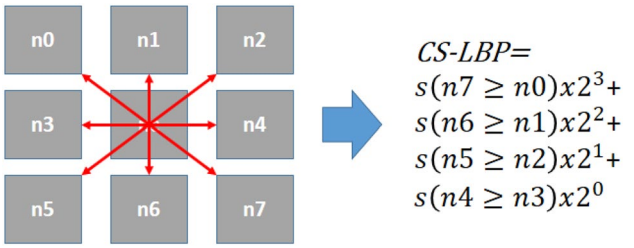

Fig. 4 CS-LBP features for neighboring 8 pixels

Input: The resized input CT image or patch (***im***) with a size of $\boldsymbol{w} \times \boldsymbol{h}$.
Output: Feature vector (***fv***) with a length of **3152**.

00: Load ***im***
01: for i=1 to $\boldsymbol{w-2}$ do
02: for j=1 to $\boldsymbol{h-2}$ do
03: Divide ***im*** into $\mathbf{3} \times \mathbf{3}$ sized overlapping blocks.
04: Assign center pixel and neighbor pixels.
05: **for** h=1 to 4 **do** // *Extract bits using signum function.*
06: $\boldsymbol{bit(h) = np(h) \geq csp(h)}$; // $\boldsymbol{np(h)}$ *is* h^{th} *neighbor pixel*
// $\boldsymbol{csp(h)}$ *is* h^{th} *center symmetric pixel*
07: **end for h**
08: $\boldsymbol{map(i,j) = \sum_{h=1}^{4} bit(h) \times 2^{h-1}}$ // *Create map image*
09: end for j
10: end for i
11: Extract the histogram of ***map*** and obtain a feature vector

Algorithm 2 CS-LBP procedure

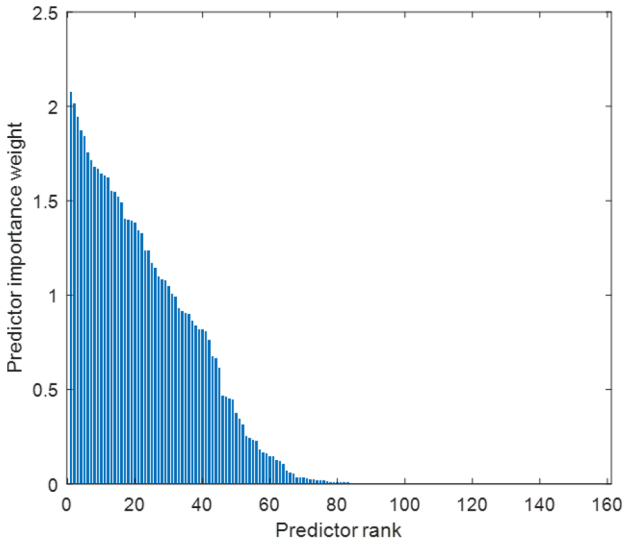

Fig. 5 The weights of the features selected with the NCA algorithm

For the NN classifier, we have used rectified linear unit (ReLU) activation function with a layer size of 25. For the optimizable classifiers kNN and SVM, Bayesian optimization [32] was used to select the best hyperparameters. The hyperparameters are indicated in Table 2. Bayesian optimization produces results according to the minimum misclassification rate. The minimum classification error changes of kNN and SVM classifiers are given in Fig. 6.

Performance Analysis

Experimental Setup

The model was implemented on the MATLAB 2021a platform, and MATLAB Classification Learner Toolbox was used in the classification process. The experiments were run on a personal computer with i5 7th-generation 7400 3.00-GHz CPU, 8-GB RAM, and 120-GB HDD on Windows 10 Pro operating system.

Table 2 Hyperparameter search ranges of kNN and SVM classifiers

Feature	Value	Feature	Value
Classifier type	kNN	Classifier type	SVM
Number of neighbors	1–380	Multiclass method	One-vs-all, One-vs-one
Distance metric	City block, Chebyshev, Correlation, Cosine, Euclidean, Hamming, Jaccard, Mahalanobis, Cubic, Spearman	Box constraint level	0.001–1000
Distance weight	Equal, Inverse, Squared inverse	Kernel scale	0.001–1000
Iteration	30	Kernel function	Gaussian, Linear, Quadratic, Cubic

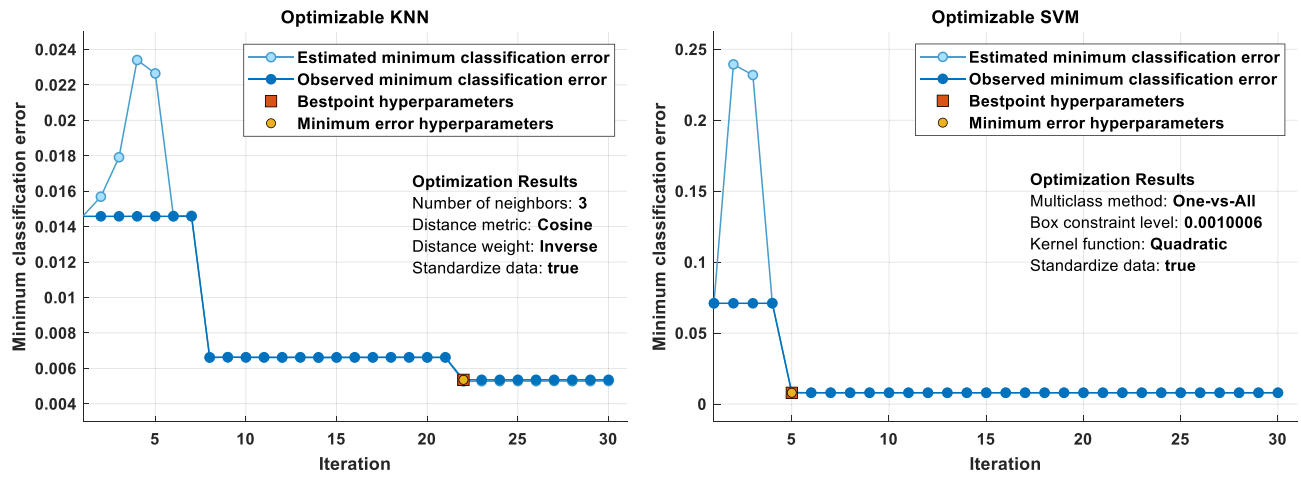

(a) Optimizable kNN **(b)** Optimizable SVM

Fig. 6 Hyperparameter search results of classifiers

Results

Confusion matrices were generated for all classifiers. Performance metrics, namely, accuracy, sensitivity, specificity, precision, *F*-measure, and geometric mean values, were obtained using true positive (TP), true negative (TN), false positive (FP), and false negative (FN) rates. Equations (4)–(9) [34, 35] were used to compute the performance parameters.

$$Accuracy = \frac{TP + TN}{TP + TN + FP + FN} \tag{4}$$

$$Sensitivity = recall = \frac{TP}{TP + FN} \tag{5}$$

$$Specifity = \frac{TN}{FP + TN} \tag{6}$$

$$Precision = \frac{TP}{TP + FP} \tag{7}$$

$$F_{\text{measure}} = \frac{2 \times precision \times recall}{precision + recall} \tag{8}$$

$$Geometric_{\text{mean}} = \sqrt{sensitivity \times specifity} \tag{9}$$

The model achieved excellent performance with all classifiers (Table 3), and kNN classifier outperforming the rest.

Confusion matrices obtained using kNN, SVM, and NN are shown in Figs. 7, 8, and 9, respectively. Again, all three classifiers demonstrated excellent accuracy with minimal misclassifications. However, kNN was the only one that did not mislabel any pathological adrenal mass as normal.

We have calculated the training and validation curve of the proposed model using the NN classifier. The number of iterations is equal to 1000, and this cure is demonstrated in Fig. 10.

Figure 10 demonstrates that there is no overfitting and the last validation accuracy is 98.81%.

Table 3 Performance metric values for all classifiers

Metrics	Classifiers		
	kNN (%)	SVM (%)	NN (%)
Accuracy	99.87	99.21	98.81
Sensitivity	99.92	99.15	98.80
Specificity	99.96	99.68	99.57
Precision	99.83	99.44	98.91
***F*-measure**	99.88	99.30	98.86
Geometric mean	99.94	99.42	99.18

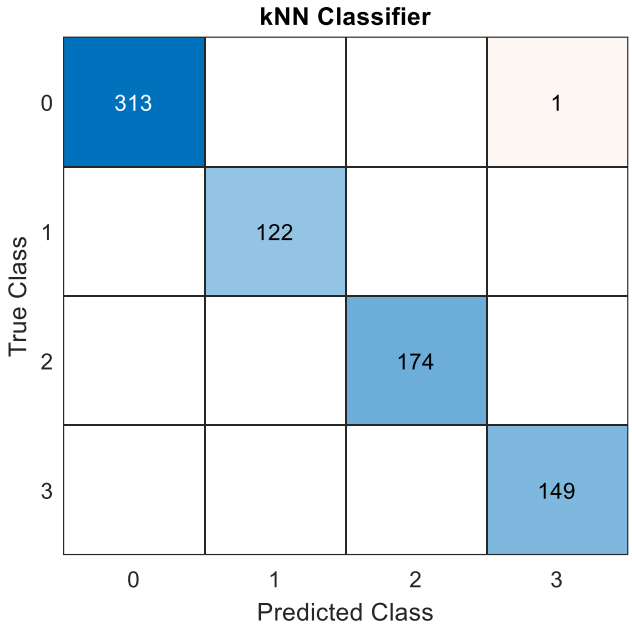

Fig. 7 Confusion matrix for kNN classifier

Discussion

CT provides important diagnostic information to clinicians that will help manage patients' medical problems. However, CT's comprehensive cross-sectional anatomical coverage often uncovers incidental findings that may not be related to the primary medical complaint. Adrenal incidentalomas are not uncommon, and there is a clinical need for its accurate

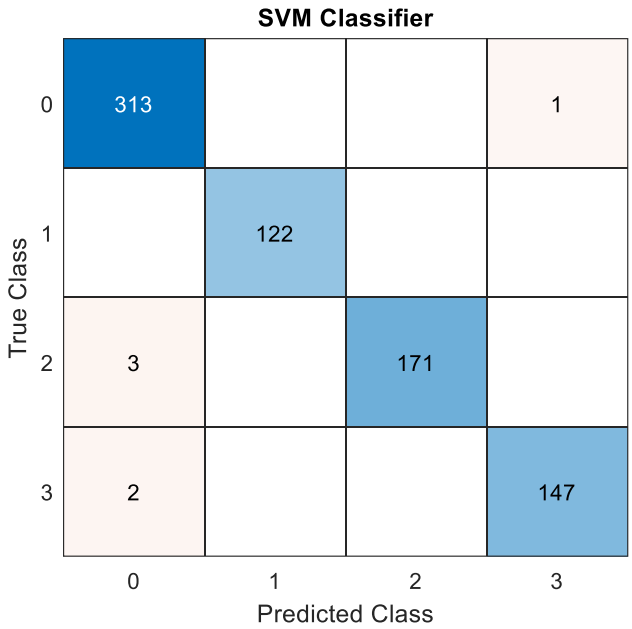

Fig. 8 Confusion matrix for SVM classifier

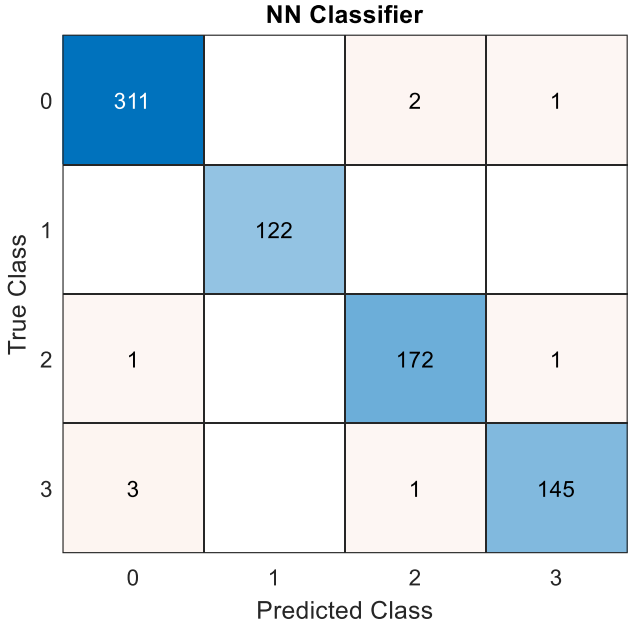

Fig. 9 Confusion matrix for NN classifier

pathological classification from among possible differential diagnoses. Prior research based on texture analysis has yielded fair to good classification performance for binary and multiclass classification combinations of adrenal pathologies. However, there still exists some risk of missing serious pathologies.

This study developed a new ML model for the four-class classification of adrenal lesions using CT images. The model achieved excellent performance when tested on a new dataset acquired and carefully annotated by medical experts for

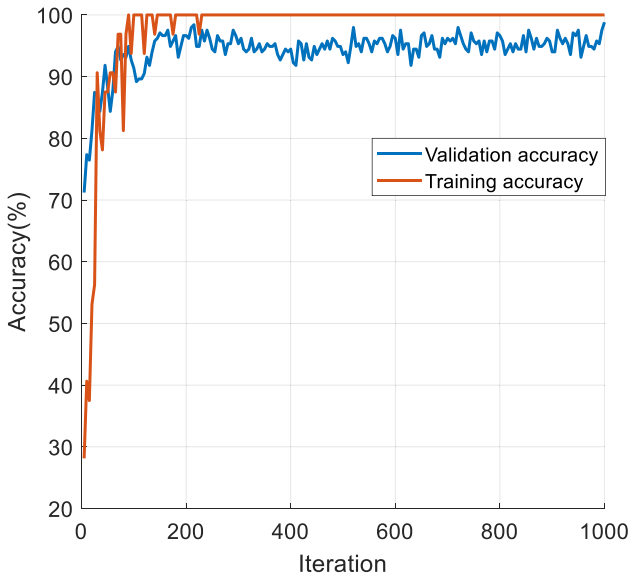

Fig. 10 Training and validation curve of the NN classifier

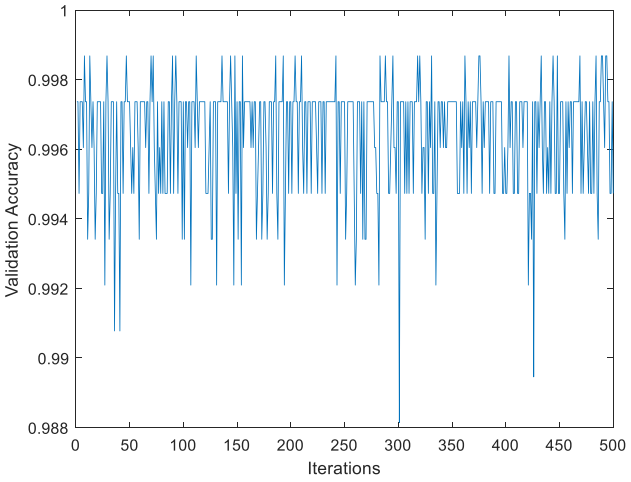

Fig. 11 Validation accuracies for each iteration

the study. Important steps of the model include (1) image preprocessing involving ROI-based image segmentation to remove extraneous data outside the body contour in the image slices that contain cross-sectional views of the adrenal glands; (2) CS-LBP function that extracted features from the main image as well as 16×16 fixed-size patches derived from the main image to construct a concatenated feature vector of length 3152; (3) NCA to select the 160 most distinctive features; and (4) classification. The best result of 99.87% accuracy was obtained using the kNN algorithm with Bayesian optimization of hyperparameters. A 10-fold CV with 500 iterations was performed to ensure the model's

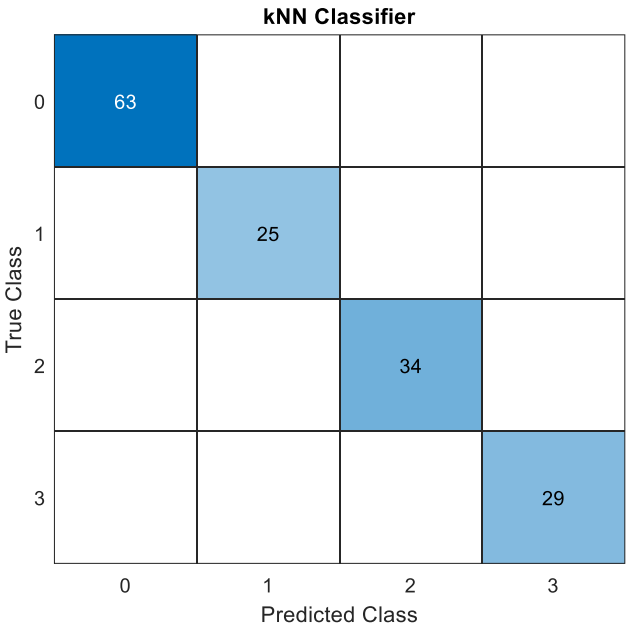

Fig. 12 Confusion matrix for 80:20 hold-out validation

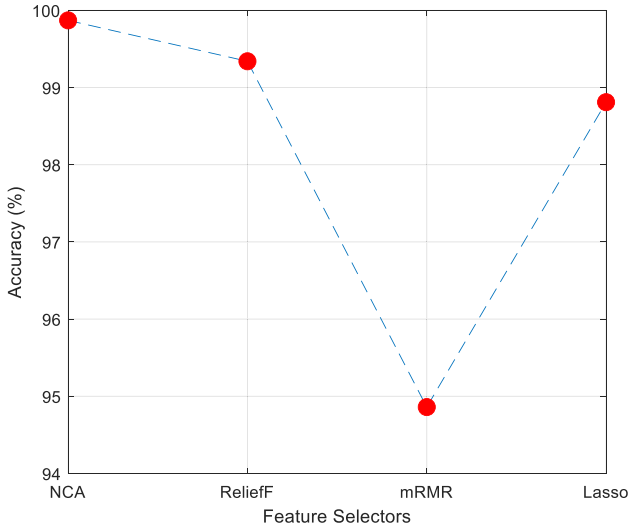

Fig. 13 The performance of feature selectors

classification performance. The validation accuracies of this test process are given in Fig. 11.

As given in Fig. 11, the developed model reached the highest validation accuracy in the first 100 iterations. Therefore, the number of iterations is set to 100. In addition to the 10-fold CV strategy, the 80:20 hold-out validation strategy was tested in the study. The developed model reached 100% classification accuracy in 80:20 hold-out validation. The confusion matrix obtained for this test is given in Fig. 12.

In the feature selection phase of the developed model, 4 different feature selectors (ReliefF, mRMR, NCA, and LASSO) were tested, and NCA was chosen as the best feature selector. A block diagram of this test process is given in Fig. 13.

To demonstrate the performance of the patch-based CS-LBP method proposed in this study, the main image-, patch image-, and main image + patch (our proposal)-based test were performed. The test results are presented in Fig. 14.

As can be seen from Fig. 13, the main + patch image-based solution achieved the best classification accuracy. In addition, Fig. 13 shows the performance of the CSLBP method. The CSLBP method has achieved over 85% accuracy, even in the main image scenario. In addition, the developed model was tested in different patch sizes and the best patch size was determined as 16 × 16. The results obtained for different patch sizes are given in Fig. 15.

The CSLBP feature extraction method is similar to the LBP feature extraction procedure [36, 37]. However, CS-LBP extracts fewer features (16 features), and these features are significant. We have used a patch-based model. Many features have been extracted since we used each patch for feature extraction. This situation causes high time complexity in the feature selection side. Therefore, we need fewer and more significant features. To reach this aim, we have used CS-LBP. Comparing CSLBP and LBP feature extraction for similar test scenarios, the accuracy value obtained is 99.87% and 99.34%, respectively, and CSLBP achieved a 0.5% higher classification result than LBP.

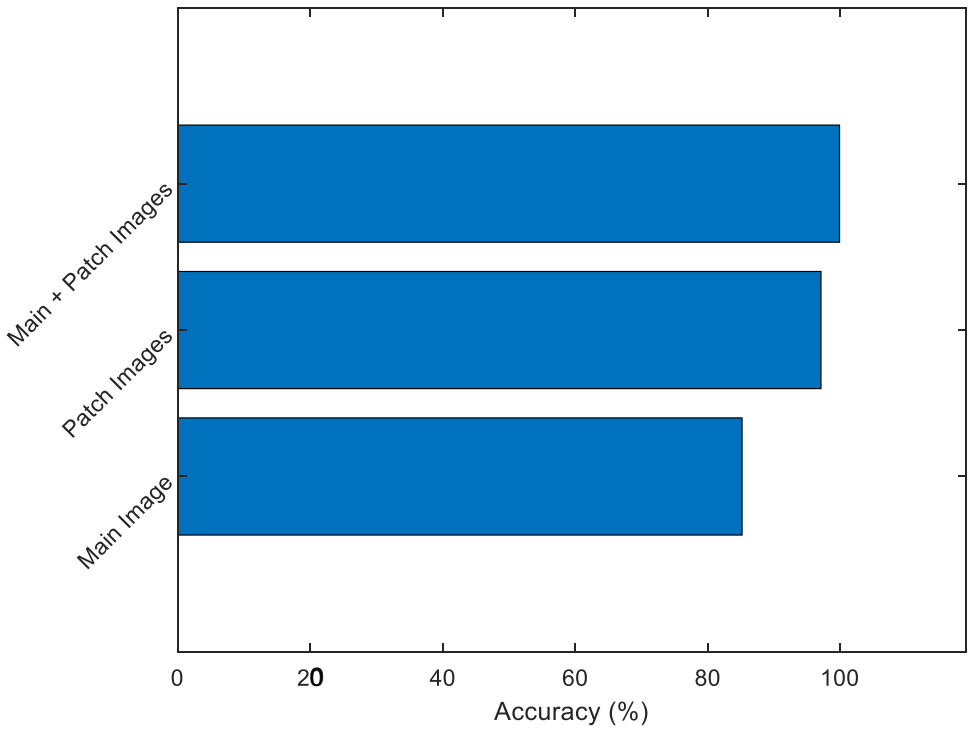

Fig. 14 Performance comparison of only main image (224 × 224), patch images (16 × 16), and main + patch images (our method). Sixteen features are extracted from the main image with the CSLBP method. For this reason, the NCA algorithm was not used in the classification scenario for the main images. In the patch image classification scenario, 3136 features were extracted and 160 features were selected with NCA

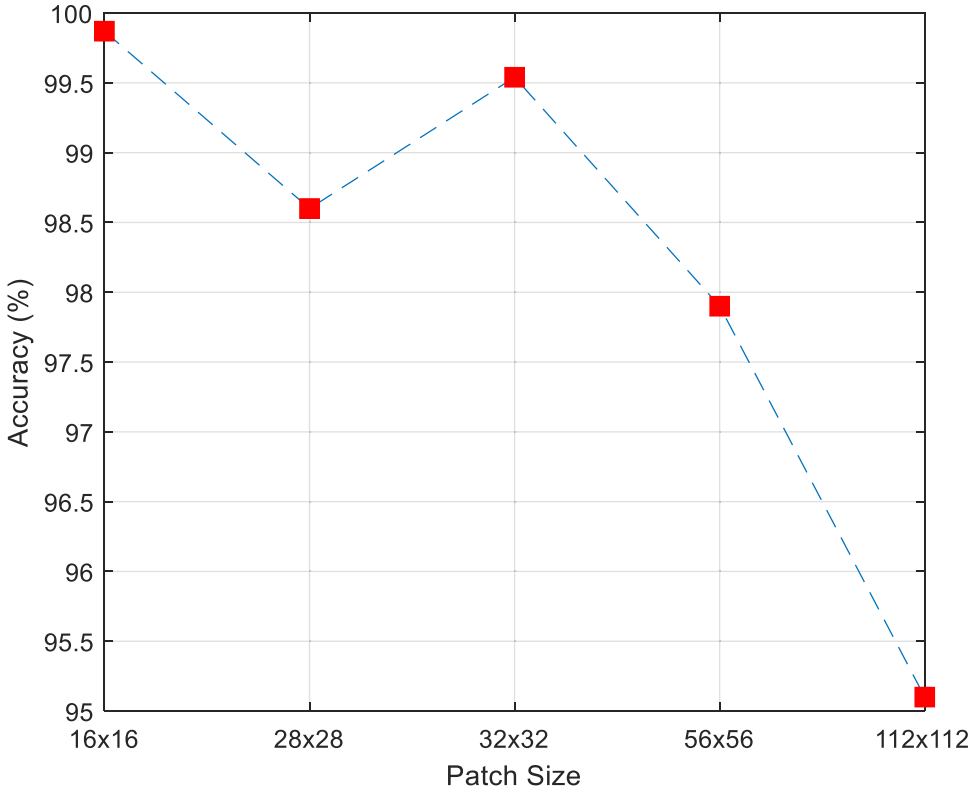

Fig. 15 Classification results for different patch sizes

In our model, there is only one misclassified observation, and it is shown in Fig. 16.

Figure 16 demonstrates that the reason for the misclassification is the color. Generally, metastasis images have light-colored structure. This image is light-colored. Therefore, the proposed model predicted this image as metastasis.

As can be seen from Fig. 16, there is one misclassified observation. Therefore, the proposed model attained 99.87% classification accuracy with 10-fold cross-validation. Using this validation, 100% classification accuracy was attained for 9-folds. Only fold 3 attained less than 100% accuracy. Fold-wise classification accuracies are shown in Fig. 17.

In this dataset, there are 759 images. The kNN classifier uses 76 observations for 9 folds (except for fold 3), and 75 observations have been used in fold 3. There is one misclassified observation in fold 3. Therefore, the classification accuracy of this fold is equal to $\left(\frac{74}{75} \cong 98.67\%\right)$.

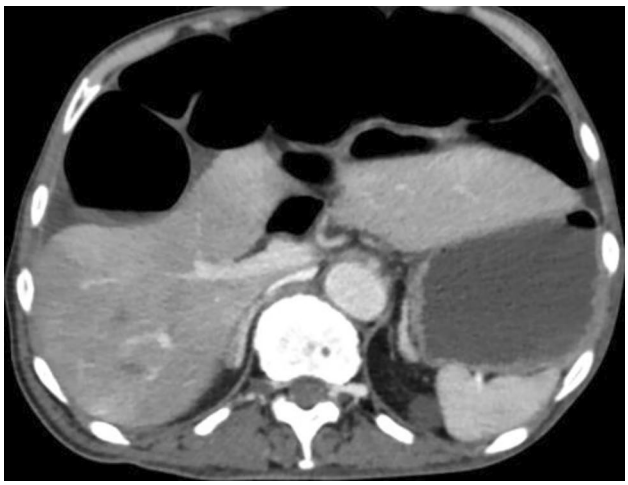

Fig. 16 The misclassified image. Real label: normal, predicted label: metastasis

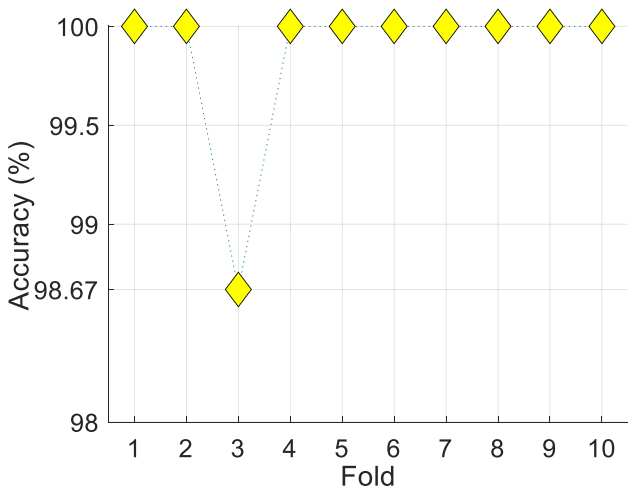

Fig. 17 Fold-wise classification accuracies of the kNN classifier

Table 4 Time complexity of the CS-LBP-based automatic classification model

Step	Time cost
ROI-based segmentation	$O(w \times h)$
Image resizing	$O(w \times h)$
Divide patches into adrenal gland image	$O(w \times h)$
Feature extraction with CS-LBP from each patch	$O(m \times n \times t)$
Feature concatenation	$O(k)$
Feature selection	$O(k)$
Classification	$O(d)$
Total	$O(3 \times w \times h + m \times n \times t + 2k + d)$

w and h are the width and height of the raw CT image, respectively. m and n are the width and height of the patches, respectively. For the developed model, m and n are 16. t is the number of patches. k is the size of the feature vector, and d is the size of the selected features

The methods used in this handcrafted ML model are simple and effective. We believe that a major contributor to the high performance lies in its patch-based operation. By dividing the main image into numerous fixed-size patches and performing secondary feature extraction on them using the same CS-LBP function, we could generate a large feature vector for downstream feature selection and classification. Compared with popular standard deep learning approaches, our method has a low computational complexity of $O(wxh + k)$ (Table 4) without compromising accuracy, which is an important consideration for clinical adoption of the model as a high-throughput CT image screening tool.

The time complexity of the proposed model is $O(w \times h + m \times n \times t + k + d)$.

We have compared our developed model with other state-of-the-art techniques for automated adrenal disease classification systems using CT images in Table 5.

Table 5 Comparison of our developed model with other automated adrenal lesion classification systems using CT images

Study	Method	Number of classes	Purpose	Subjects	Performance matrices (%)
Elmohr et al. [10]	Intensity- and geometry-based texture feature extraction and random forest classifier	2 (tumor and control)	Differentiating large adrenal cortical tumors	54	Accuracy: 82.00 Sensitivity: 81.00 Specificity: 83.00
Stanzione et al. [11]	Radiomic feature extraction, recursive feature selection, and extra tree classification	2 (solid lesion and control)	Classifying indeterminate solid adrenal lesions	55	Precision: 92.00 Recall: 91.00 F_1-score: 91.00
Yi et al. [38]	Radiomic feature extraction, Lasso feature selection	2 (lipid-poor adenoma and subclinical pheochromocytoma)	Differentiating pheochromocytoma and lipid-poor adenoma in adrenal incidentalomas	265	AUC: 90.70
Moawad et al. [12]	Texture feature extraction, recursive feature elimination, and random forest classification	2 (lesion and control)	Differentiating indeterminate small adrenal tumors	181	AUC: 85.00 Sensitivity: 84.20 Specificity: 71.40
Yi et al. [14]	Texture feature extraction, feature selection, and logistic multiple-regression classification	2 (subclinical pheochromocytoma and lipid-poor adenoma)	Differentiating pheochromocytoma and lipid-poor adenoma in adrenal incidentalomas	108	Accuracy: 94.40 Sensitivity: 86.20 Specificity: 97.50
Robinson-Weiss et al. [39]	Deep learning-based segmentation and classification	2 (normal and adrenal masses)	Adrenal gland segmentation and normal/adrenal mass classification	251 and 991	Development dataset Dice: 0.80 (normal) 0.84 (masses) Sensitivity: 83 Specificity: 89 Test dataset Dice: 0.89 (normal) 0.89 (masses) Sensitivity: 69 Specificity: 91
Our method	Image segmentation, texture feature extraction using exemplar CS-LBP, NCA-based feature selection, hyperparameter-tuned kNN classification	4 (normal, pheochromocytoma, lipid-poor adenoma, and metastasis)	Classifying adrenal gland lesions	96	Accuracy: 99.87 Sensitivity: 99.92 Specificity: 99.96 Precision: 99.83 F-measure: 99.88 Geometric mean: 99.94

It can be noted from Table 5 that the presented exemplar CS-LBP-based model attained the highest classification performance of more than 99% with 96 subjects. These results (see Table 5) denote that the presented model scored the highest in classifying four classes (the rest are two classes). Our proposed fixed patch-batched operation captured minute features from the CT images and contributed to the highest classification results. Also, hyperparameter optimization has increased the classification ability of the used kNN and SVM classifiers.

The highlights of this study are as follows:

- A new four-class dataset has been created to study the classification of adrenal gland lesions.
- The new patch-based CS-LBP feature extraction approach demonstrated uniform success with a classification accuracy of 99.87%, 99.21%, and 98.81% using kNN, SVM, and NN classifiers, respectively.
- The patch-based operation with the ML method will highlight the subtle features without increasing the time complexity. Hence, our proposed method is efficient.
- A 10-fold CV with 100 iterations was performed to ensure the robustness of the model.
- The model's excellent classification performance and low time complexity support its adoption as an efficient triage for high-throughput screening of voluminous CT image data to improve radiologists' workflow. In addition, the undemanding computational requirements favor its application for remote expert consultation.

Conclusions

This study developed a new handcrafted ML model for automatically classifying adrenal gland CT images into four clinically relevant labels: normal, pheochromocytoma, lipid-poor adenoma, and metastasis. The CT images were divided into 16×16 fixed-size patches, and feature extraction was performed using the CS-LBP method. Extracted features were chosen using NCA and classified using the kNN classifier to obtain the optimum-performing model. Our proposed method obtained the best classification accuracy of 99.87% with low computational complexity. The limitation of this study is that we have used only 96 subjects (59 males, 37 females). In the future, we plan to validate our proposed system with more subjects belonging to *four* classes (normal, pheochromocytoma, lipid-poor adenoma, and metastasis).

Data Availability The public data presented in this study are available from https://www.kaggle.com/turkertuncer/surrenal-image-dataset.

Declarations

Conflict of Interest The authors declare no competing interests.

References

1. Jason DS, Oltmann SC: Evaluation of an adrenal incidentaloma. Surgical Clinics 99:721-729, 2019
2. Korivi BR, Elsayes KM: Cross-sectional imaging work-up of adrenal masses. World journal of radiology 5:88, 2013
3. Bharwani N, et al.: Adrenocortical carcinoma: the range of appearances on CT and MRI. American journal of roentgenology 196:W706-W714, 2011
4. Lattin Jr GE, et al.: From the radiologic pathology archives: adrenal tumors and tumor-like conditions in the adult: radiologic-pathologic correlation. Radiographics 34:805-829, 2014
5. Romeo V, et al.: The role of dynamic post-contrast T1-w MRI sequence to characterize lipid-rich and lipid-poor adrenal adenomas in comparison to non-adenoma lesions: preliminary results. Abdominal Radiology 43:2119-2129, 2018
6. Schieda N, Alrashed A, Flood TA, Samji K, Shabana W, McInnes MD: Comparison of quantitative MRI and CT washout analysis for differentiation of adrenal pheochromocytoma from adrenal adenoma. American Journal of Roentgenology 206:1141-1148, 2016
7. Allen BC, Francis IR: Adrenal imaging and intervention. Radiologic Clinics 53:1021-1035, 2015
8. Zhang G-M-Y, Shi B, Sun H, Jin Z-Y, Xue H-D: Differentiating pheochromocytoma from lipid-poor adrenocortical adenoma by CT texture analysis: feasibility study. Abdominal Radiology 42:2305-2313, 2017
9. Spartalis E, et al.: Metastatic carcinomas of the adrenal glands: from diagnosis to treatment. Anticancer research 39:2699-2710, 2019
10. Elmohr M, et al.: Machine learning-based texture analysis for differentiation of large adrenal cortical tumours on CT. Clinical radiology 74:818. e811-818. e817, 2019
11. Stanzione A, et al.: Handcrafted MRI radiomics and machine learning: classification of indeterminate solid adrenal lesions. Magnetic Resonance Imaging 79:52-58, 2021
12. Moawad AW, Ahmed A, Fuentes DT, Hazle JD, Habra MA, Elsayes KM: Machine learning-based texture analysis for differentiation of radiologically indeterminate small adrenal tumors on adrenal protocol CT scans. Abdominal Radiology:1–11, 2021
13. Romeo V, et al.: Characterization of adrenal lesions on unenhanced MRI using texture analysis: a machine-learning approach. Journal of Magnetic Resonance Imaging 48:198-204, 2018
14. Yi X, et al.: Adrenal incidentaloma: machine learning-based quantitative texture analysis of unenhanced CT can effectively differentiate sPHEO from lipid-poor adrenal adenoma. Journal of Cancer 9:3577, 2018
15. Jayapriya K, Jacob IJ, Mary N: Person re-identification using prioritized chromatic texture (PCT) with deep learning. Multimedia Tools and Applications 79:29399-29410, 2020
16. Dharma D: Coral reef image/video classification employing novel octa-angled pattern for triangular sub region and pulse coupled convolutional neural network (PCCNN). Multimedia Tools and Applications 77:31545-31579, 2018
17. Marée R, Geurts P, Piater J, Wehenkel L: Biomedical image classification with random subwindows and decision trees. Proc. International Workshop on Computer Vision for Biomedical Image Applications: City
18. Poyraz AK, Dogan S, Akbal E, Tuncer T: Automated brain disease classification using exemplar deep features. Biomedical Signal Processing and Control 73:103448, 2022

19. Tuncer T, Dogan S, Baygin M, Acharya UR: Tetromino pattern based accurate EEG emotion classification model. Artificial Intelligence in Medicine 123:102210, 2022
20. Thanh DNH, Prasath VB, Hieu LM, Hien NN: Melanoma skin cancer detection method based on adaptive principal curvature, colour normalisation and feature extraction with the ABCD rule. Journal of Digital Imaging 33:574-585, 2020
21. Demir S, et al.: Automated knee ligament injuries classification method based on exemplar pyramid local binary pattern feature extraction and hybrid iterative feature selection. Biomedical Signal Processing and Control 71:103191, 2022
22. Barua PD, et al.: Multilevel deep feature generation framework for automated detection of retinal abnormalities using OCT images. Entropy 23:1651, 2021
23. Dosovitskiy A, et al.: An image is worth 16×16 words: transformers for image recognition at scale. arXiv preprint arXiv:201011929, 2020
24. Tolstikhin I, et al.: MLP-Mixer: an all-MLP architecture for vision. arXiv preprint arXiv:210501601, 2021
25. Singh R, Athisayamani S: Banana leaf diseased image classification using novel HEAP auto encoder (HAE) deep learning. Multimedia Tools and Applications 79:30601-30613, 2020
26. Goldberger J, Hinton GE, Roweis S, Salakhutdinov RR: Neighbourhood components analysis. Advances in neural information processing systems 17:513-520, 2004
27. Peterson LE: *K*-nearest neighbor. Scholarpedia 4:1883, 2009
28. Vapnik V: The support vector method of function estimation: Springer, 1998
29. Vapnik V: The nature of statistical learning theory: Springer science & business media, 2013
30. Wan EA: Neural network classification: a Bayesian interpretation. IEEE Transactions on Neural Networks 1:303-305, 1990
31. Mary NAB, Dharma D: Coral reef image classification employing improved LDP for feature extraction. Journal of Visual Communication and Image Representation 49:225-242, 2017
32. Frazier PI: A tutorial on Bayesian optimization. arXiv preprint arXiv:180702811, 2018
33. Ojala T, Pietikainen M, Maenpaa T: Multiresolution gray-scale and rotation invariant texture classification with local binary patterns. IEEE Transactions on pattern analysis and machine intelligence 24:971-987, 2002
34. Powers DM: Evaluation: from precision, recall and *F*-measure to ROC, informedness, markedness and correlation. arXiv preprint arXiv:201016061, 2020
35. Warrens MJ: On the equivalence of Cohen's kappa and the Hubert-Arabie adjusted Rand index. Journal of classification 25:177-183, 2008
36 Ani Brown Mary N, Dejey D: Classification of coral reef submarine images and videos using a novel Z with tilted Z local binary pattern (Z⊕ TZLBP). Wireless Personal Communications 98:2427-2459, 2018
37. Ani Brown Mary N, Dharma D: A novel framework for real-time diseased coral reef image classification. Multimedia Tools and Applications 78:11387-11425, 2019
38. Yi X, et al.: Radiomics improves efficiency for differentiating subclinical pheochromocytoma from lipid-poor adenoma: a predictive, preventive and personalized medical approach in adrenal incidentalomas. EPMA Journal 9:421-429, 2018
39. Robinson-Weiss C, et al.: Machine learning for adrenal gland segmentation and classification of normal and adrenal masses at CT. Radiology:220101, 2022

Authors and Affiliations

Suat Kamil Sut[1] · Mustafa Koc[2] · Gokhan Zorlu[3] · Ihsan Serhatlioglu[3] · Prabal Datta Barua[4,5] · Sengul Dogan[6] · Mehmet Baygin[7] · Turker Tuncer[6] · Ru-San Tan[8,9] · U. Rajendra Acharya[10,11,12]

Suat Kamil Sut
sut_kml@hotmail.com

Mustafa Koc
mkoc@firat.edu.tr

Gokhan Zorlu
gkzorlu@gmail.com

Ihsan Serhatlioglu
iserhatlioglu@firat.edu.tr

Prabal Datta Barua
prabal.barua@usq.edu.au

Mehmet Baygin
mehmetbaygin@ardahan.edu.tr

Turker Tuncer
turkertuncer@firat.edu.tr

Ru-San Tan
tanrsnhc@gmail.com

U. Rajendra Acharya
aru@np.edu.sg

[1] Department of Radiology, Adiyaman Training and Research Hospital, Adiyaman, Turkey

[2] Department of Radiology, Faculty of Medicine, Firat University, Elazig, Turkey

[3] Department of Biophysics, Faculty of Medicine, Firat University, Elazig, Turkey

[4] School of Business (Information System), University of Southern Queensland, Toowoomba, QLD 4350, Australia

[5] Faculty of Engineering and Information Technology, University of Technology Sydney, Sydney, NSW 2007, Australia

[6] Department of Digital Forensics Engineering, College of Technology, Firat University, Elazig, Turkey

[7] Department of Computer Engineering, College of Engineering, Ardahan University, Ardahan, Turkey

[8] Department of Cardiology, National Heart Centre, Singapore, Singapore

[9] Duke-NUS Medical School, Singapore, Singapore

[10] Department of Electronics and Computer Engineering, Ngee Ann Polytechnic, Singapore 599489, Singapore

[11] Department of Biomedical Engineering, School of Science and Technology, SUSS University, Singapore, Singapore

[12] Department of Biomedical Informatics and Medical Engineering, Asia University, Taichung, Taiwan